Comput Mech (2018) 61:55–70
https://doi.org/10.1007/s00466-017-1467-3

ORIGINAL PAPER

Effect of microstructure on the elasto-viscoplastic deformation of dual phase titanium structures

Tugce Ozturk[1] · **Anthony D. Rollett**[1]

Received: 12 January 2017 / Accepted: 9 August 2017 / Published online: 22 August 2017

Abstract The present study is devoted to the creation of a process–structure–property database for dual phase titanium alloys, through a synthetic microstructure generation method and a mesh-free fast Fourier transform based micromechanical model that operates on a discretized image of the microstructure. A sensitivity analysis is performed as a precursor to determine the statistically representative volume element size for creating 3D synthetic microstructures based on additively manufactured Ti–6Al–4V characteristics, which are further modified to expand the database for features of interest, e.g., lath thickness. Sets of titanium hardening parameters are extracted from literature, and The relative effect of the chosen microstructural features is quantified through comparisons of average and local field distributions.

Keywords FFT based elasto-viscoplastic micromechanical model · Synthetic microstructure generation · 3D materials science · Dual phase titanium alloys · Additive manufacturing

1 Introduction

Powder-bed based additive manufacturing (AM) of metallic components, in which a 3D shape is written into successive layers of powder using an electron or laser beam under computer control, is increasingly being implemented to produce structural parts. Having a wide range of application in the aerospace, automotive and medical industries, AM of titanium components is now valued because of the near-net shape and reduced machining cost advantages of the technique [1]. However, since titanium is an allotropic element that can exist in more than one crystallographic form depending on the chemo-thermo-mechanical process history, the rapid cooling inherent in the AM technique makes the prediction of the component microstructure and the mechanical properties challenging. For instance, the room temperature alpha, or hexagonal close-packed (hcp), phase can co-exist with the high temperature (above 883 °C) beta, or body-centered cubic (bcc), phase when alloyed with elements such as aluminum and oxygen that stabilize alpha, or elements such as vanadium and molybdenum that stabilize beta [2]. Furthermore, the dual-phase alloys exhibit a wide variety of distinct microstructures such as fully lamellar, duplex, or fully equiaxed, with varying texture evolution as a function of the thermomechanical history [3–5], all of which influence the mechanical properties.

While there are established process–structure–property relationships for different alpha/beta titanium alloys in literature [6], the large thermal gradients and cooling rates inherent in powder-bed metal AM makes for challenges in the prediction of mechanical properties. The beam scanning though successive layers means that each location experiences a series of thermal spikes, whose precise sequence depends on location in the part. The thermal history also involves slow changes in temperature mainly as a function of build height, resulting in anisotropic and heterogeneous microstructures within each AM component. For instance, it has been shown that depending on the beam power/velocity parameters, a Ti–6Al–4V microstructure can change from martensitic or fine acicular α' structure at the high cooling rate top of the build height, into fine $\alpha + \beta$ lamellae, Widmanstätten, or a mix-

✉ Tugce Ozturk
toztur@gmail.com

Anthony D. Rollett
rollett@andrew.cmu.edu

[1] Department of Materials Science and Engineering, Carnegie Mellon University, 5000 Forbes Avenue, Pittsburgh, PA 15213, USA

ture of colonized lamellar α and coarse acicular α' phases at the slower cooling rate, middle of the build height sections [7–9]. Furthermore, the solidification structure is affected by the cooling rate and thermal gradient dependent prior β morphology and size, which can be varied substantially through control of the process conditions [10,11]. As the α lath thickness and prior β grain size increases with decreased cooling rate, the ultimate tensile strength (UTS) and yield strength (YS) values are known to decrease [3]. This in turn causes a mechanical property anisotropy between the exterior AM regions with finer microstructures, and the coarser interior regions [12].

Since microstructural features are known to determine the microscopic and macroscopic mechanical behavior, it is important to quantify and model the relationships between the properties and the prior β grain size and morphology, the thickness and size of individual α laths, and the volume fraction and orientation distribution of the phases. For this purpose, in this study we present a new methodology to generate dual phase titanium microstructures, a statistically representative volume element (SRVE) simulation size requirement analysis, a synthetic microstructure database, and the micromechanical response modeling of the structures through the full-field fast Fourier transform (FFT) based elasto-viscoplastic technique as to quantify the relative effect of individual microstructure descriptors.

2 Dual-phase titanium representative structures with varying microstructural features

Microstructure based crystal plasticity models are extensively operated to simulate the elasto-viscoplastic behavior of polycrystalline materials by using the grain maps as input data. When the interest is in the investigation of structure–property relationships through large dataset analysis, microstructural characterization such as surface mapping via EBSD or 3D mapping via synchrotron based techniques can be time and budget consuming. One possible solution to increase the microstructure database is the computational approach via digital generation of statistically representative microstructures. Various methods have been developed for three-dimensional statistical microstructure reconstruction, such as the 3D Voronoi tessellation, where a volume is filled with random points and then the point joining line perpendicular bisecting planes are tessellated such that the volume is divided into Voronoi cells, each of which corresponds to a unique grain [13]. Other methods involve packing spheres with a lognormal volume distribution into a domain, and then using the center of masses as tessellation initiation points [14], or using ellipsoid distributions to approximate the grain size and shape distributions that exist in the real microstructures for determining Voronoi seed points [15–17].

Thanks to ongoing developments in packing algorithms and general computational capability, digital representation of grain-scale microstructures has extended to more complex materials. For dual-phase titanium, examples include: beta processed titanium where the lamellar structure is homogenized for simulation efficiency [18]; a case in which the alpha/beta structure is assumed to be a colony grain structure with random orientation assignment [19]; a microstructure in which grains are assumed to be cubes, and the lamellar duplex structure is homogenized for meshing efficiency [20]; and, a case in which the bimodal primary alpha+lamellar colony characteristics are represented through size distributions [21]. Although these structures are shown to be statistically representative in various ways, the computational expense limited what could be accomplished with finite element based micromechanical modeling that explicitly describe the lamellar morphology, individual α laths, or Widmanstätten characteristics, because the two-phase lamellar structures require a large element count and correspondingly large number of degrees of freedom. The present paper sidesteps this issue by using a meshless, FFT-based full field micromechanical model formulated on a regular grid, which can compute full field solutions directly on image of microstructures with >100 prior β grains and $>50{,}000$ α laths.

For the purpose of generating statistically representative multi phase digital microstructures to specifically address AM titanium, a set of statistics is extracted from the additively manufactured Ti–6Al–4V literature. This suggests using an average columnar or equiaxed prior β width of 50–200 μm [22,23], an average α lath size of 0.5–2 μm [24,25], and a preferred prior β texture of (001) with a Burgers orientation relationship (BOR) between the phases [22,26,27]. The strong texture arises from the near-universal observation of columnar solidification in this alloy, which is unsurprising in view of the unusually small freezing range in this alloy [28]. Since the objective is forming a microstructure-mechanical response database, initial beta microstructures, Fig. 1, are created via DREAM.3D [29] based on the parent grain size statistics, which are then modified to include the features of interest, i.e., the lamellae, by using a transformation phase insertion algorithm. The algorithm consists of operating on each of the parent phase voxel structures to insert additional grains that represent the second (hexagonal) phase by calculating the center of mass and spherical equivalent radius of each parent grain for controlling the lath width and length, until a given number of daughter grains are successfully generated. The daughter grain orientation is defined by rotation from the parent grain in accordance with the applicable orientation relationship. For titanium, the BOR, where the close-packed $\{011\}$ plane of the bcc lattice is parallel to the close-packed (0001) plane of the hcp lattice, and the $\langle 111\rangle$ direction in the bcc lattice is parallel to

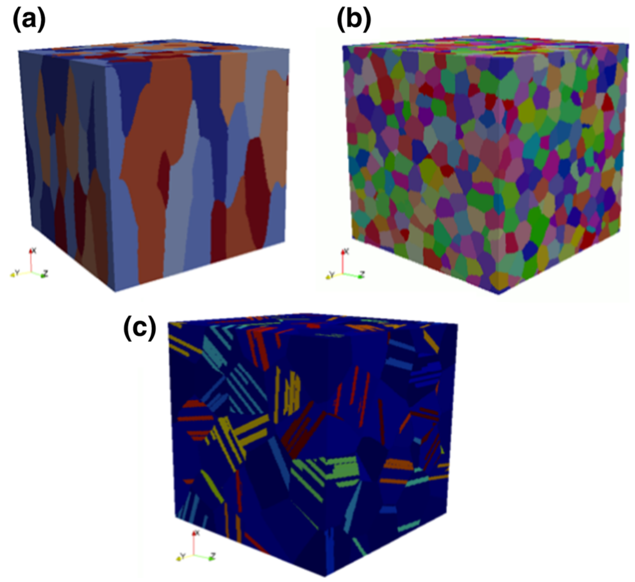

Fig. 1 Examples of digital microstructures. **a** A preferred (001) axis columnar prior β structure. **b** An equiaxed prior β structure. **c** A dual-phase β matrix–α lath structure

Table 1 Burgers orientation relationship and axis/angle pair for $\beta->\alpha$ transformation

	Axis	Angle
$(1\ 1\ 0)_\beta//(0\ 0\ 0\ 1)_\alpha$ $[\bar{1}\ 1\ \bar{1}]_\beta//[1\ 1\ \bar{2}\ 0]_\alpha$	(−0.067, −0.791, −0.607)	125.77
$(1\ 1\ 0)_\beta//(0\ 0\ 0\ 1)_\alpha$ $[1\ \bar{1}\ \bar{1}]_\beta//[1\ 1\ \bar{2}\ 0]_\alpha$	(0.762, −0.642, 0.085)	90.41
$(\bar{1}\ 0\ 1)_\beta//(0\ 0\ 0\ 1)_\alpha$ $[1\ \bar{1}\ 1]_\beta//[1\ 1\ \bar{2}\ 0]_\alpha$	(−0.244, 0.769, 0.590)	56.6
$(\bar{1}\ 0\ 1)_\beta//(0\ 0\ 0\ 1)_\alpha$ $[1\ 1\ 1]_\beta//[1\ 1\ \bar{2}\ 0]_\alpha$	(0.244, 0.769, −0.590)	56.6
$(0\ 1\ 1)_\beta//(0\ 0\ 0\ 1)_\alpha$ $[1\ 1\ \bar{1}]_\beta//[1\ 1\ \bar{2}\ 0]_\alpha$	(0.594 −0.307 −0.742)	69.73
$(0\ 1\ 1)_\beta//(0\ 0\ 0\ 1)_\alpha$ $[\bar{1}\ 1\ \bar{1}]_\beta//[1\ 1\ \bar{2}\ 0]_\alpha$	(0.194, −0.375, −0.906)	129.73
$(0\ 1\ \bar{1})_\beta//(0\ 0\ 0\ 1)_\alpha$ $[\bar{1}\ 1\ 1]_\beta//[1\ 1\ \bar{2}\ 0]_\alpha$	(0.431, 0.833, 0.345)	159.73
$(0\ 1\ \bar{1})_\beta//(0\ 0\ 0\ 1)_\alpha$ $[1\ 1\ 1]_\beta//[1\ 1\ \bar{2}\ 0]_\alpha$	(0.872, 0.451, 0.187)	140.26
$(1\ 0\ 1)_\beta//(0\ 0\ 0\ 1)_\alpha$ $[\bar{1}\ 1\ 1]_\beta//[1\ 1\ \bar{2}\ 0]_\alpha$	(−0.379, −0.120, −0.917)	147.49
$(1\ 0\ 1)_\beta//(0\ 0\ 0\ 1)_\alpha$ $[1\ 1\ \bar{1}]_\beta//[1\ 1\ \bar{2}\ 0]_\alpha$	(−0.244, −0.769, −0.590)	56.6
$(1\ \bar{1}\ 0)_\beta//(0\ 0\ 0\ 1)_\alpha$ $[1\ 1\ \bar{1}]_\beta//[1\ 1\ \bar{2}\ 0]_\alpha$	(−0.762, −0.642, −0.085)	90.41
$(1\ \bar{1}\ 0)_\beta//(0\ 0\ 0\ 1)_\alpha$ $[1\ 1\ 1]_\beta//[1\ 1\ \bar{2}\ 0]_\alpha$	(−0.837, −0.071, −0.542)	114.54

the $\langle 11\bar{2}0\rangle$ direction in the hcp lattice, results in 12 possible variants and each habit plane/direction produces a distinct orientation. The set of axis-angle pair misorientations from parent bcc to daughter hcp grains is given in Table 1. In order to illustrate how the parent/daughter orientation relationship is maintained in the algorithm, columnar retained beta, inserted alpha laths, and BOR between the marked beta grain and alpha lath for a 256 × 256 × 256 voxel digital microstructure is shown in Fig. 2. To create the dual phase titanium microstructure/mechanical response database, multiple structures with varying features are generated via the insertion method explained above. In Fig. 3, statistically representative microstructure generation steps and a subset of the synthetic structures are illustrated.

3 FFT-based spectral micromechanical modeling

Starting with the works of Sachs and Taylor [30,31], mechanical behavior models evolved over time. The Sachs model (or the lower-bound model) assumes a homogeneous stress field in which all grains experience same stress tensor, and compatibility is violated at grain boundaries, whereas Taylor (or the upper-bound model) assumes uniform strain in the microstructure in which all grains undergo same strain tensor, and stress equilibrium fails at grain boundaries. Neither of these methods takes account of the interactions inside the microstructure, so a more accurate method called self-consistent (SC) modeling was developed. Based on the analysis of Eshelby [32], the SC approach treats each ellipsoidal shaped grain as an inclusion that is embedded inside a homogeneous reference medium (the microstructure domain), and then strain is calculated as an average field within each grain [33,34]. Molinari showed that the deformed texture prediction is in good agreement with known experimental results [33]. Since self-consistent formulation is a mean field method, conventionally, small-scale finite element techniques are used to simulate the local mechanical response of complex microstructures. Clearly, the finite element method requires meshing, which results in a system with a large number of degrees of freedom. One alternative to the finite element method (FEM) is the Fast Fourier Transform (FFT) based formulation, introduced by Moulinec and Suquet as a tool for full-field simulation of mechanical response of polycrystalline materials. In general, the FFT algorithm computes the stress and strain fields at each point on a regular, discretized grid based on the crystallographic orientation (and associated anisotropy) of the point when the microstructure is subjected to macroscopic loading [35]. It uses a microstructural image with orientation information as direct input, and requires periodic unit cells and boundary conditions. Since the method does not require meshing, the

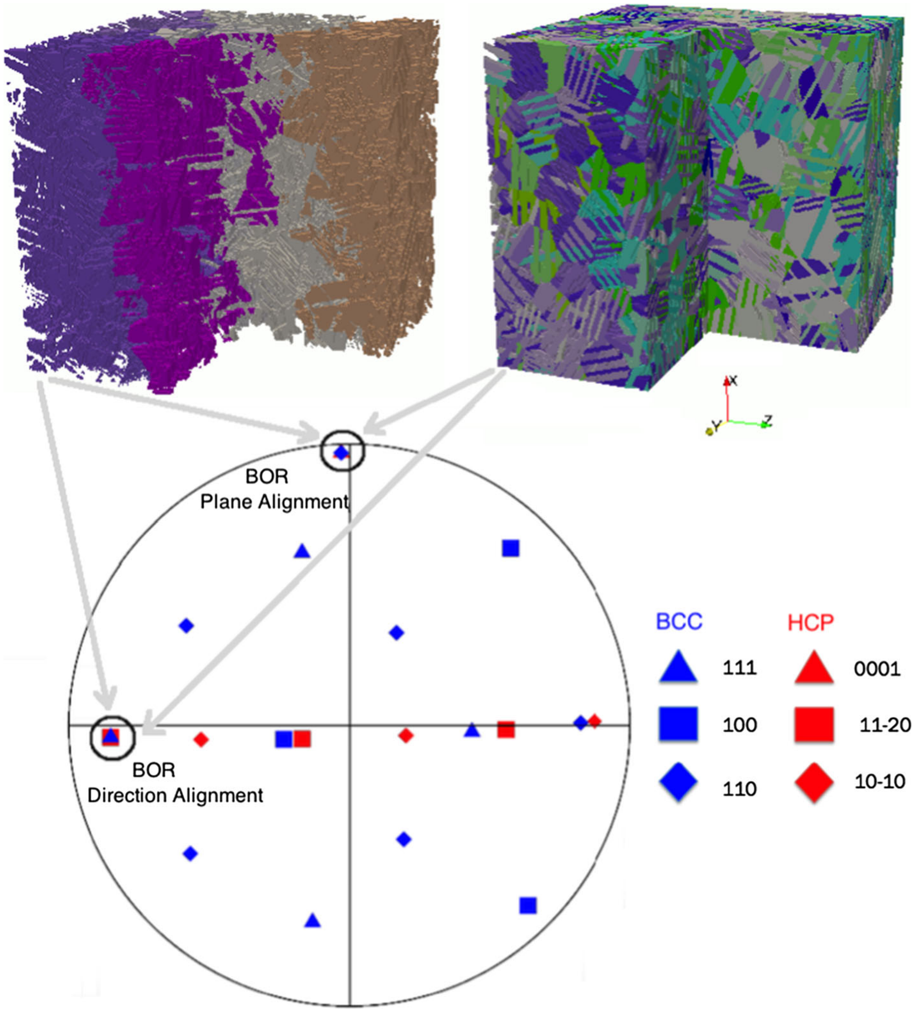

Fig. 2 Columnar retained beta grains, inserted alpha laths and the Burgers OR (BOR) between the marked beta grain and alpha lath for a 256 × 256 × 256 digital microstructure. The grains are *colored* by Euler angles on an arbitrary scale

calculation is computationally efficient and is able to manage a large number of degrees of freedom typically involved in the description of complex microstructures [35,36]. Prakash and Lebensohn compared FFT with FEM and demonstrated that the FFT computations scale as NlogN (for N is the number of grid points), whereas FEM typically scales as N^2, which means it is computationally more expensive for large problems [36]. Lebensohn showed that for linear systems, FFT results provide similar accuracy as the SC approximation, with the additional advantage of giving local field values [37] i.e., it can resolve intragranular gradients. While the utilization of a regular grid prevails computational advantages, the existence of inherent Fourier method numerical instabilities, such as the observed Gibbs phenomenon at discontinuities, can cause undesired stress oscillations. This phenomenon can be reduced by avoiding single voxels, and by spreading the discontinuity features throughout the domain. In the FFT based algorithm, the multi-phase behavior is captured through defining the model properties for each phase individually, and calculating the n-site grain interactions both within one phase and between all phases. Elastic, viscoplastic and elasto-viscoplastic deformation regimes are all formulated in the algorithm [38,39]. For these regimes, the problem is solved iteratively using an initial guess for the local strain field values, and then adopting a convergence criterion that relates to the fulfillment of the equilibrium condition. The convergence criterion depends on the spatial resolution and the complexity of the microstructure, and the linearity of the model. For instance, for the elastic regime the convergence criterion of 10^{-4} is found to be appropriate, however for the non-linear, viscoplastic regime, a smaller convergence criterion of 10^{-5}–10^{-6} is suggested [38]. The elastic, viscoplastic and elasto-viscoplastic deformation regimes are detailed in the following sections.

3.1 Elastic formulation

Assuming periodic boundary conditions across the elastically heterogeneous representative volume element (RVE), which is subjected to an average strain **E**, a reference medium is prepared by defining an initial homogeneous reference stiffness tensor on a regular grid of N points by $C^0_{ijkl} = \frac{1}{N}\sum C_{ijkl}(x)$.

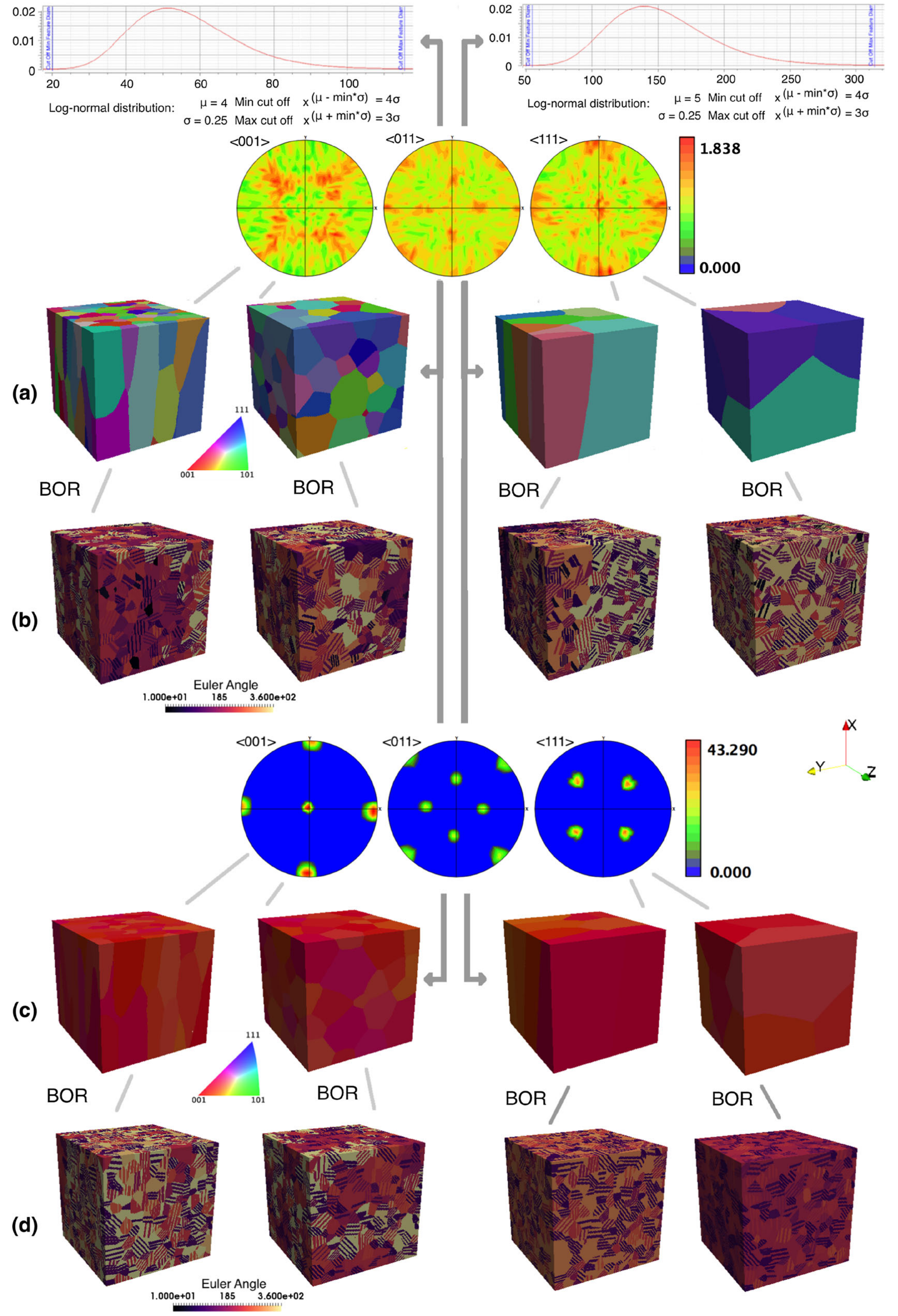

Fig. 3 Illustration of the synthetic microstructure generation for two different parent prior β grain size distributions, average 50 µm on the *left two* and average 145 µm on the *right two*: **a** randomly orientated columnar and equiaxed β parent grains; **b** two phase structure after 50% α insertion following the BOR; **c** (001) textured columnar and equiaxed β parent grains; **d** two phase structure after 50% α insertion following the BOR

Taking $\varepsilon(\mathrm{x})$ as the local strain, $\sigma(\mathrm{x})$ as the local stress and C(x) as the local stiffness tensor, the local problem can be written in terms of the constitutive equation (Hooke's law) and the equilibrium condition across the boundary of two adjacent grains.

$$\begin{aligned} &\sigma_{ij}(x) = C_{ijkl}(x)\varepsilon_{kl}(x) \quad in\ RVE \\ &\sigma_{ij,j}(x) = 0 \quad in\ RVE \end{aligned} \tag{1}$$

For small strain compatibility condition $\varepsilon_{kl}(x) = \frac{(u_{k,l}(x)+u_{l,k}(x))}{2}$, where u is the displacement gradient, and the local fluctuations in stress $\tau_{ij} = (C_{ijkl} - C^0_{ijkl}) : \varepsilon(x)$, the problem becomes

$$\sigma_{ij}(x) = C^0_{ijkl}\, u_{k,l}(x) + \tau_{ij}(x) \tag{2}$$

where τ_{ij} is the local deviation from the average stress field that can be calculated iteratively using the fluctuation in stiffness and local strain. Combining Eq. (2), and the equilibrium condition $\sigma_{ij,j} = 0$ gives

$$\tau_{ij,j}(x) + C^0_{ijkl}\, u_{k,lj}(x) = 0. \tag{3}$$

In real space, $\tau_{ij,j}(x)$ can be thought as a fictitious body force. In order to solve Eq. (3) by Green's method, G is defined as

$$\hat{G}_{ik} = [C^0_{ijkl}\,\omega_l\,\omega_j]^{-1} = \hat{A}^{-1}_{ik} \tag{4}$$

where ω is frequency in Fourier space and $\hat{A}^{-1}\hat{A} = I$. Taking the Fourier transform of equation (3) results in

$$F\left[\sum_{lj} C^0_{ijkl}\frac{\partial u_k}{\partial x_l\,\partial x_j}\right] = -F(\tau_{ij,j}(x)). \tag{5}$$

In Fourier space, the fictitious body force field $\tau_{ij,j}$ and the strain field $\varepsilon_{ij}(x)$ [40] can be written as

$$\begin{aligned} &F(\tau_{ij,j}(x)) = \sum_j i\,\omega_j\,\hat{\tau}_{ij} = i\sum_j \hat{\tau}_{ij}\,(\omega)\,\omega_j \\ &F(\varepsilon_{ij}(x)) = i\,\hat{u}_i(\omega)\,\omega_j. \end{aligned} \tag{6}$$

For $\hat{\Gamma}^0_{ijkl} = -\hat{G}_{ik}\,\omega_l\,\omega_j$ (symmetrization), Eqs. (4), (5) and (6) give

$$\hat{\hat{\varepsilon}}_{ij}(\omega) = \hat{\Gamma}^0_{ijkl}\,\hat{\tau}_{ij}(\omega). \tag{7}$$

Inverse Fourier transformation converts the perturbation field τ_{ij} into real space, which is replaced in Eq. (2) to calculate the stress field.

Algorithm for elastic FFT

The algorithm is initialized with $\hat{\hat{\varepsilon}}(x) = 0$ and $\sigma^0(x) = C^0 : \mathbf{E}$, and then the local stress–strain fluctuations are calculated iteratively [38].

a. Macroscopic average strain, determined from the boundary conditions is initialized as the elastic strain at each grid point.
b. Local stress at each grid point is calculated from the strain using Hooke's law.
c. Polarization field is calculated through Green's method and Fourier transform.
d. Stress equilibrium and convergence is tested.
e. New stress–strain fields are updated.
f. Steps b–e are repeated until convergence.

3.2 Viscoplastic formulation

Following Molinari [33], the stress tensor is decomposed into deviatoric stress and hydrostatic pressure components as

$$\sigma_{ij} = \sigma'_{ij} - p\delta_{ij} \tag{8}$$

where σ' is the deviatoric and p is the hydrostatic pressure components. Thus, equilibrium and incompressibility conditions become

$$\begin{aligned} &\sigma_{ij,j} = \tilde{\sigma}_{ij,j} = \sigma'_{ij,j} + p_{,i} = 0 \\ &v_{k,k} = 0 \end{aligned} \tag{9}$$

where v is velocity.

In the plastic regime, either the secant or tangent approach can be used to calculate the stiffness. In this formulation, tangent approach is chosen where $E_{\tan} = \frac{d\sigma}{d\varepsilon}$.

The local constitutive equation then becomes

$$\sigma'(x) = M^{tg^{-1}}(x) : d(x) + S^o(x) \tag{10}$$

where M^{tg}(x) is the local tangent compliance (thus $M^{tg^{-1}}$ is tangent stiffness, and will be denoted as L^{tg}), d(x) is local strain rate, and S^o is the back-extrapolated stress term coming from Taylor expansion at a fixed point.

Since the relationship between stress and strain is not linear in plastic region, stiffness cannot be simply averaged as in the elastic solution to find the reference medium value. The homogenous reference medium is described in terms of a tangent behavior as

$$\Sigma' = L^{tg}_o : D + S^{oo} \tag{11}$$

where L^{tg}_o *and* S^{oo} are respectively the stiffness and back-extrapolated stress of the medium.

In this viscoplastic FFT algorithm, the initial values of the strain-rate field are assigned using a Taylor guess of $\dot{\tilde{\varepsilon}}_{ij}(x) = 0$, hence $\dot{\varepsilon}_{ij}(x) = \dot{\mathbf{E}}$ as the convergence is tested at each grid point. For **n** is the slip plane normal, **b** is the slip direction, $R = \begin{pmatrix} b_1 & n_1 & x_1 \\ b_2 & n_2 & x_2 \\ b_3 & n_3 & x_3 \end{pmatrix}$ is the transformation matrix from slip system axes to crystal axes, $m_{ij} = \frac{1}{2}(b_i\, n_j + b_j\, n_i)$ is the Schmid tensor, and $\varepsilon_{ij}^{slip} = \begin{pmatrix} 0 & \frac{\gamma}{2} & 0 \\ \frac{\gamma}{2} & 0 & 0 \\ 0 & 0 & 0 \end{pmatrix}$ is the strain tensor in slip level, transformation of a shear γ from slip system to crystal axes can be written as

$$\begin{aligned} \varepsilon_{ij}^{crystal} &= R_{1i}\, R_{2j}\, \varepsilon_{12}^{slip} + R_{2i}\, R_{1j}\, \varepsilon_{21}^{slip} \\ \varepsilon_{ij}^{crystal} &= \frac{1}{2}(b_i\, n_j + b_j\, n_i)\gamma \;\; = m_{ij}\, \gamma \end{aligned} \tag{12}$$

and the resolved shear stress on slip plane and slip direction is given by

$$\begin{aligned} \tau &= \sigma_{12}^{slip} = R_{1i}\, R_{2j}\, \sigma_{ij}^{crystal} \\ \tau &= b_i\, n_j\, \sigma_{ij}^{crystal} = m_{ij}\, \sigma_{ij}^{crystal}. \end{aligned} \tag{13}$$

Because slip plane normal and slip direction are perpendicular to each other, $\mathbf{n} \perp \mathbf{b}$, the trace of the Schmid tensor is zero, tr(m) $= b_k\, n_k = 0$. Thus, trace of crystal system strain tensor is also zero as tr(ε) = tr(m) = 0, i.e. the crystal system strain tensor should be traceless as a result of incompressibility. Superimposition of shear over the slip systems gives total strain rate of the grid point as

$$\dot{\varepsilon}_{ij} = \sum_{s}^{N} m_{ij}^{s} \dot{\gamma}^{s}. \tag{14}$$

Both Lebensohn [38] and Tomé [41] describe the local incompressible viscoplastic constitutive behavior by means of the rate-sensitive approach,

$$\dot{\gamma}^{s} = \dot{\gamma}_{o} \left(\frac{\tau^{s}}{\tau_{o}^{s}} \right)^{n} = \dot{\gamma}_{o} \left(\frac{m_{kl}^{s}\, \sigma_{kl}}{\tau_{o}^{s}} \right)^{n}. \tag{15}$$

Substituting $\dot{\gamma}^{s}$ into Eq. (15) gives the non-linear constitutive equation as

$$\dot{\varepsilon}_{ij} = \dot{\gamma}_{o} \sum_{s} m_{ij}^{s} \left(\frac{m_{kl}^{s}\, \sigma_{kl}}{\tau_{o}^{s}} \right)^{n}. \tag{16}$$

Note that the tangent stiffness is the derivative of stress with respect to strain. Thus, the local compliance $M^{tg}(x)$ denoted in the constitutive Eq. (10), summed over all potentially active slip systems becomes

$$M^{tg}(x) = n\dot{\gamma}_{0} \sum_{s} \frac{m^{s}(x) \bigotimes m^{s}(x)}{\tau_{0}^{s}(x)} \left(\frac{m^{s}(x) : \sigma'(x)}{\tau_{0}^{s}(x)} \right)^{(n-1)} \tag{17}$$

where $\tau_{0}^{s}(x)$ is the critical resolved shear stress, $\dot{\gamma}_{0}$ is the normalization factor and n is the reciprocal of the rate sensitivity. $\tau_{0}^{s}(x)$ and $m^{s}(x)$ are related to the crystal deformation by slip. For the local non-linear constitutive equation $\sigma'(x) = M^{tg^{-1}}(x) : d(x) + S^{o}(x)$, the stress equation, including both the deviatoric and the hydrostatic pressure parts becomes

$$\sigma_{ij} = L_{ijkl}^{tg} : d_{kl} + S_{kl}^{o} - p\, \delta_{ij} \tag{18}$$

where $L^{tg} = M^{tg^{-1}}$ and δ_{ij} is Kronecker delta. For $\tilde{L}^{tg} = L^{tg} - L_{o}^{tg}$ and $\tilde{S}^{o} = S^{o} - S^{oo}$, taking the derivative of the stress constitutive equation and equating to zero to satisfy the equilibrium condition results in

$$\sigma_{ij,j} = 0 = S_{ij,j}^{oo} - p_{,i} + \left(\tilde{L}_{ijkl}^{tg}\, d_{kl} + \tilde{S}_{ij}^{o} \right)_{j} + L_{o_{ijkl}}^{tg}\, d_{kl,j} \tag{19}$$

where $L_{o_{ijkl}}^{tg}\, d_{kl,j} = \frac{1}{2}(L_{o_{ijkl}}^{tg}\, \nu_{k,lj} + L_{o_{ijkl}}^{tg}\, \nu_{l,kj})$ because of the strain rate part of compatibility condition. Here, it is assumed that $L_{o_{ijkl}}^{tg}$ has minor symmetry. Thus, $L_{o_{ijkl}}^{tg} = L_{o_{ijlk}}^{tg}$, and $L_{o_{ijkl}}^{tg}\, d_{kl,j} = \frac{1}{2}(L_{o_{ijkl}}^{tg}\, \nu_{k,lj} + L_{o_{ijlk}}^{tg}\, \nu_{l,kj})$ As repeated indices are dummy indices, for $l = k$ and k = l, compatibility condition is

$$L_{o_{ijkl}}^{tg}\, d_{kl,j} = \frac{1}{2} \left(L_{o_{ijkl}}^{tg}\, \nu_{k,lj} + L_{o_{ijkl}}^{tg}\, \nu_{k,lj} \right) = L_{o_{ijkl}}^{tg}\, \nu_{k,lj}. \tag{20}$$

Calling $(\tilde{L}_{ijkl}^{tg}\, d_{kl} + \tilde{S}_{ij}^{o}) = \tau_{ij}$, the final system of differential equations to be solved becomes

$$\begin{aligned} & L_{o_{ijkl}}^{tg}\, \nu_{k,lj}(x) + \tau_{ij,j}(x) - p_{,i}(x) = 0 \; in \; RVE \\ & \nu_{k,k}(x) = 0 \; in \; RVE \end{aligned} \tag{21}$$

Periodic BCs across RVE.

Similar to the elastic case that is explained in Sect. 3.1, the polarization field is calculated using the Green's method and FFT formalism.

Algorithm for viscoplastic FFT

The algorithm is initialized with strain rate $\dot{\tilde{\varepsilon}}_{ij}(x) = 0$, and then the local stress–strain fluctuations are calculated iteratively [38].

a. Reference medium stiffness L^0 is initialized in terms of an average tangent behavior.
b. Local stress at each grid point is calculated by solving the constitutive relation numerically via Newton–Raphson method.
c. Deviatoric stress, perturbation field and pressure field is calculated in Fourier space.
d. Stress and strain-rate fields are calculated from the constitutive equation.
e. Polarization field is calculated through Green's method and Fourier transform.
d. Stress equilibrium and convergence is tested.
e. New stress–strain fields are updated.
f. Steps b–e are repeated until convergence.
k. If the convergence is satisfied, the orientation and hardening parameters for each slip system are updated.

3.3 Elasto-viscoplastic formulation

An infinitesimal strain version of the FFT formulation in the elasto-viscoplastic regime was presented recently [39]. The solution in the elasto-viscoplastic regime involves the combined Hooke's law for the elastic part and Euler implicit time discretization for the plastic part. Briefly, the constitutive equation of giving the strain field is defined as

$$\varepsilon^{total}(x) = \varepsilon^e(x) + \varepsilon^p(x). \tag{22}$$

Equation 22 can also be written as

$$\varepsilon^{total}(x) = C^{-1}(x) : \sigma(x) + \varepsilon^{p,t}(x) + \dot{\varepsilon}^p(x, \sigma)\,\Delta t \tag{23}$$

where

$$\dot{\varepsilon}^p(x) = \dot{\gamma}_o \sum_s m^s_{ij} \left(\frac{m^s_{kl}\,\sigma_{kl}}{\tau^s_o}\right)^n. \tag{24}$$

Similar to the elastic and viscoplastic cases, the field fluctuations are defined, and then the the polarization field, which is the divergence of the perturbation field, is calculated iteratively using the Green's method and FFT formalism as explained in Sect. 3.1.

Algorithm for elasto-viscoplastic FFT

The algorithm is initialized with the total strain $\varepsilon^{total}(x) = \varepsilon^e(x)$ as the total plastic strain is zero, and then the local stress–strain fluctuations are calculated iteratively [39].

a. Local fluctuation is established via $\tau_{ij}(x) = \sigma_{ij}(x) - C^0_{ijkl}\,u_{k,l}(x)$, and combined with equilibrium condition.
b. Local stress at each grid point is calculated by solving the constitutive equations.
c. Polarization field is calculated through Green's method and Fourier transform.
d. Stress equilibrium and convergence is tested iteratively.
e. New stress–strain fields are updated.
f. If the convergence is satisfied and if $\varepsilon^{p,t}(x) \neq 0$, the orientation and hardening parameters for each slip system are updated.

3.4 Orientation and hardening updates

Once the convergence criterion is satisfied and the equilibrium condition is is fulfilled, the microstructure needs to be updated for the deformation induced changes in viscoplastic and elasto-viscoplastic regimes. The first update is for the local orientation, which is simply the difference between the local rigid body rotation rate and the local plastic rotation rate. Mathematically, local reorientation rate is defined as

$$w_{ij}(x) = \left[\dot{w}_{ij}(x) - \dot{w}^p_{ij}(x)\right] \tag{25}$$

for local rigid body rotation rate $\dot{w}_{ij} = \frac{1}{2}(v_{i,j}(x) - v_{j,i}(x))$ and plastic rotation rate $\dot{w}^p_{ij}(x) = \sum_{s=1}^{N_s} \alpha^s(x)\dot{\gamma}^s(x)$ with $\gamma^s(x)$ local shear rate and $\alpha^s(x)$ local skewsymmetric Schmid tensor [38].

The second update is for work and latent hardening, which denotes the rate of change in critical resolved shear stress (CRSS) of a primary slip system for the former or the change in CRSS of a secondary slip system for the latter. The CRSS update should be performed according to a hardening law. For this work, a modified version of the Voce [42] hardening model is used with the assumption of only self-hardening (no latent hardening). Modified Voce hardening is characterized by an evolution of the threshold stress with accumulated shear strain in the form of

$$\hat{\tau}^S = \tau_0^S + \left(\tau_1^S + \theta_1^S\,\Gamma\right)\left(1 - \exp\left(-\Gamma\left|\frac{\theta_0^S}{\tau_1^S}\right|\right)\right) \tag{26}$$

giving four parameters for each slip system in each individual phase, where τ_0^S is the initial critical resolved shear stress (CRSS), τ_1^S is the initial hardening rate, θ_0^S is the asymptotic hardening rate and θ_1^S is the back-extrapolated CRSS. Voce hardening is an empirical model, and since it does not have any temperature or strain rate sensitive terms it is intended to extract parameters from a single stress–strain dataset.

3.5 Model parameters

In order to extract the hardening parameters by matching the simulated viscoplastic self-consistent response with the experimental measurements, the multi-parameter optimization algorithm of Gockel [43] and Mandal [44] is utilized

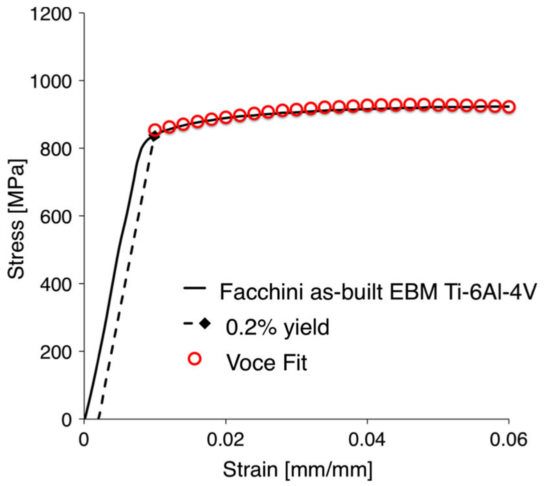

Fig. 4 Electron beam melted, as built Ti–6Al–4V stress–strain [46] fit for extracting modified Voce hardening parameters

for this study. The optimization is based on a non-linear least-squares formulation, to iteratively fit the experimental data by minimizing the summed square of the difference between the measured value and the fitted value for each strain increment. The degree of the fit is quantified by a mean error percentage and mean root mean square error (RMSE). Since titanium is a dual phase material, parameter optimization is performed on both phases simultaneously by simulating the response for assigned phase fractions and initial parameter guesses. In this study, the slip induced plastic deformation of the alpha and beta phases is modeled by individual slip systems and their relative CRSS ratios of 1:0.7:3 [45] for the basal:prism:pyramidal $\langle c + a\rangle$ systems of the hcp phase, and CRSS ratios of 0.3:0.3:0.3 for the $\{110\}\langle 111\rangle$:$\{112\}\langle 111\rangle$:$\{123\}\langle 111\rangle$ systems of the bcc phase. A set of modified Voce hardening parameters are extracted from a reported set of AM Ti–6Al–4V tensile data [46] by fitting the stress–strain curve for bcc and hcp phases simultaneously via this technique, Fig. 4, by identifying the onset of plastic deformation using a 0.2% offset line. For the elastic regime, the stiffness values reported by Stapleton et al. [47] are used. Both the elastic and plastic model parameters are listed in Table 2. It is important to note that the material parameters are chosen as the basis for all the structures, and it is possible to implement different hardening models and parameters without changing the elasto-viscoplastic algorithm.

4 Domain size sensitivity analysis results

In the elasto-viscoplastic regime, the deformation is described by a combination of linear (Hooke's law) and non-linear (rate-sensitive approach) relationships. In the elastic regime, the mechanical response is found to be nearly insensitive to the domain size when a few shells of the nearest neighbor grains are included in the simulation [48]. However, it is expected that the non-linear relationship in the plastic regime might cause higher contrast between different cell size domains as a result of n-site non-linear grain interactions. Since large simulations are computationally expensive, it is important to define the smallest statistically representative volume element (SRVE) size without sacrificing the convergence of effective and/or local properties. For instance, the grain size influence on surface roughening has been investigated, revealing an inverse relationship between convergence speed and grain size [49]. It has also been shown that the deviation from the applied strain is more sensitive to grain interactions and less so on grain self-orientation, causing local distribution to be more sensitive to domain size than macroscopic behavior [50]. Since the FFT algorithm calculates homogenized properties from the full-field values, it allows for a thorough domain size sensitivity study.

In choosing a set of microstructures for the domain size analysis, the size of the parent β grains, the lath thickness and fraction of α laths, the orientation distribution and Fourier grid point resolution are all taken into account; so that numerous dual-phase simulation structures are categorically generated, Fig. 5. Although the modeled field values converge to almost the same values when the grid resolution is changed from 1 to 8 µm/voxel for randomly oriented equiaxed grains, Fig. 6, as the lath thickness feature is cho-

Table 2 Bcc and hcp elastic constants and hardening parameters that are used in the micromechanical model

Elastic constants (GPa)	C_{11}	C_{12}	C_{13}	C_{33}	C_{44}
bcc	130	90	90	130	65
hcp	143	110	90	177	40

Modified Voce hardening parameters (MPa)	τ^0	τ^1	θ^0	θ^1
bcc (for all slip modes)	41.09	99.62	971.27	1.6
hcp (basal)	184.95	56.75	1160	−18.9
hcp (pryramidal)	264.21	56.75	1160	−18.9
hcp (prismatic $\langle a + c\rangle$)	792.63	56.75	1160	−18.9

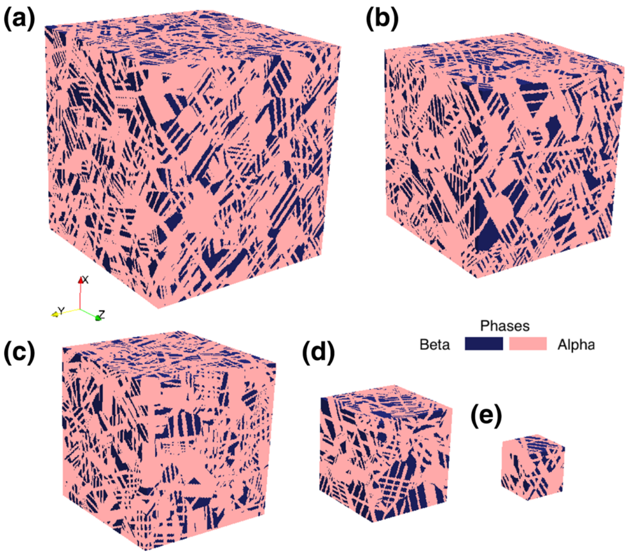

Fig. 5 Phase maps for generated synthetic 80% α dual-phase microstructures of 256^3, 216^3, 196^3, 128^3 and 64^3 domain sizes

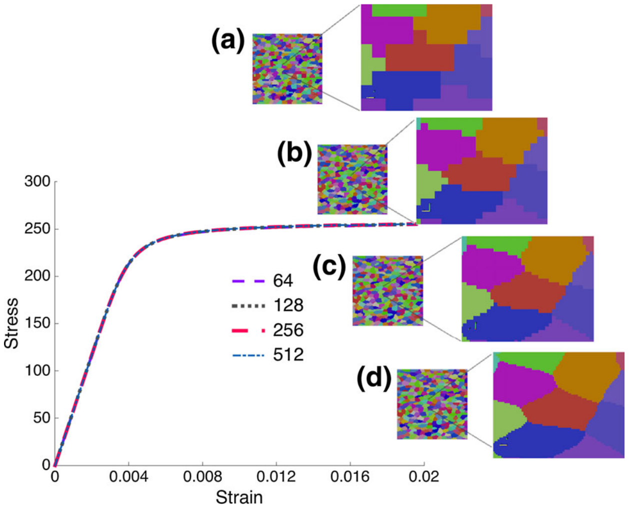

Fig. 6 Stress–strain curves for similarly deforming randomly oriented equiaxed structures with Fourier point resolution of (*a*) 8 µm/voxel, 64^3 domain; (*b*) 4 µm/voxel, 128^3 domain; (*c*) 2 µm/voxel, 256^3 domain; (*d*) 1 µm/voxel, 512^3 domain

sen as 1–2 µm in this study, the Fourier grid point resolution is taken as 1 µm/voxel in all directions. In order to obtain the highest level of microstructural heterogeneity, the parent grain size is chosen as the largest, 145 µm average with columnar morphology, lath thickness is chosen as the thickest, 2 µm average, the daughter fraction is chosen as the highest, 80%, and the orientation distribution is chosen as random with the expectation that these extreme attributes would result in higher domain size sensitivity.

Using the model parameters listed in Table 2, structures were deformed to 5% strain with combined strain/stress boundary conditions. Note that since the strong phase α fraction is 14% less than the experimental Ti–6Al–4V data that was used for hardening parameter extraction, the macroscopic field values do not match with Fig. 4. Both the local and homogenized values converged at 216^3 simulation size, Fig. 7. Hence, 216^3 is chosen to be the SRVE, and all of the microstructures reported in Sect. 5 are generated accordingly.

5 Microstructure sensitivity analysis results

In order to investigate the effect of microstructure on mechanical properties, the microscopic and macroscopic fields are simulated for a total of 56 conditions, Fig. 8. 36 distinct microstructures with varying prior β grain sizes and morphologies, individual α lath thicknesses and sizes, phase volume fractions, and orientation distributions were generated. Furthermore, the effect of uniaxial loading direction is examined by modeling the response of 20 different Widmanstätten structures for tensile deformation parallel and perpendicular to the long grain axis (axis ODF) direction. Using combined stress/strain boundary conditions, elasto-viscoplastic deformation of the generated microstructure database, Fig. 8, was modeled with deformation step increments of 0.0001, up to total 4% macroscopic tensional strain. The convergence criterion to satisfy the equilibrium condition with $<10^{-6}$ error is achieved in between iteration 20–30 for all cases. This dataset will be publicly available in the future; until then the readers are encouraged to contact the authors if they wish to access the data, e.g. for testing reduced dimensionality representations of the microstructures via spatial correlation statistics, for extracting properties using principal component analysis (PCA), and eventually for building data-driven models using linear regression, polynomial regression and/or machine learning based techniques that can accurately predict the mechanical response based on a given microstructure.

The macroscopic stress–strain response is summarized in Fig. 9, where the effect of α fraction for for 50 µm randomly oriented columnar prior β parent structures is shown in Fig. 9a, the effect of lath thickness for 150 µm randomly oriented and textured columnar prior β parent structures is shown in Fig. 9b, and the effect of prior β grain size, grain morphology and orientation distribution for 53% α is shown in Fig. 9c. The response is found to be the most sensitive to α phase fraction and the prior β orientation distribution, such that the increase in α phase enhances the tensile strength, and the increased magnitude of prior β (001) texture decreases the tensile strength. This can be explained by α being the harder phase, and the prior β (001) texture being the soft direction for bcc, with restricted transformed α orientation space as a result of BOR. The phase fraction variability is further investigated by comparing the contribution of each phase against the behavior of dual-phase composite structure, Fig. 10, in order to check if the observed alpha fraction effect is

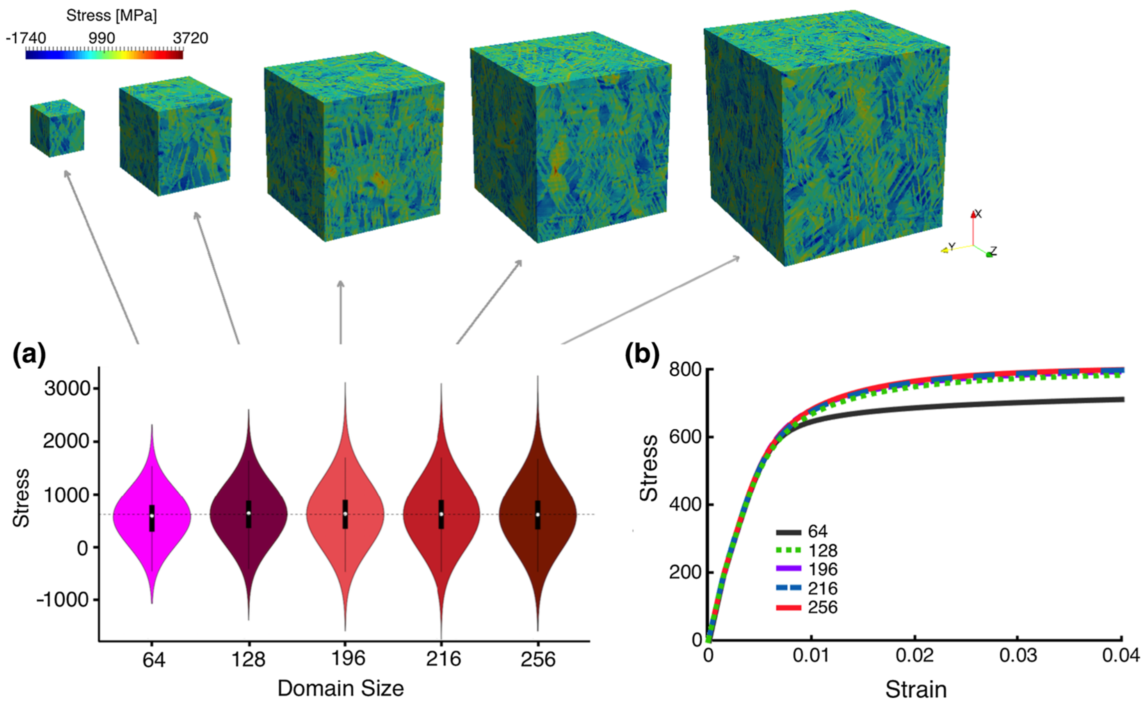

Fig. 7 Domain size sensitivity analysis using 64^3, 128^3, 196^3, 216^3 and 256^3 microstructures: **a** full-field stress (component along the loading direction) violin plots and stress distributions at 4% strain for each domain; **b** macroscopic stress–strain curve for each domain

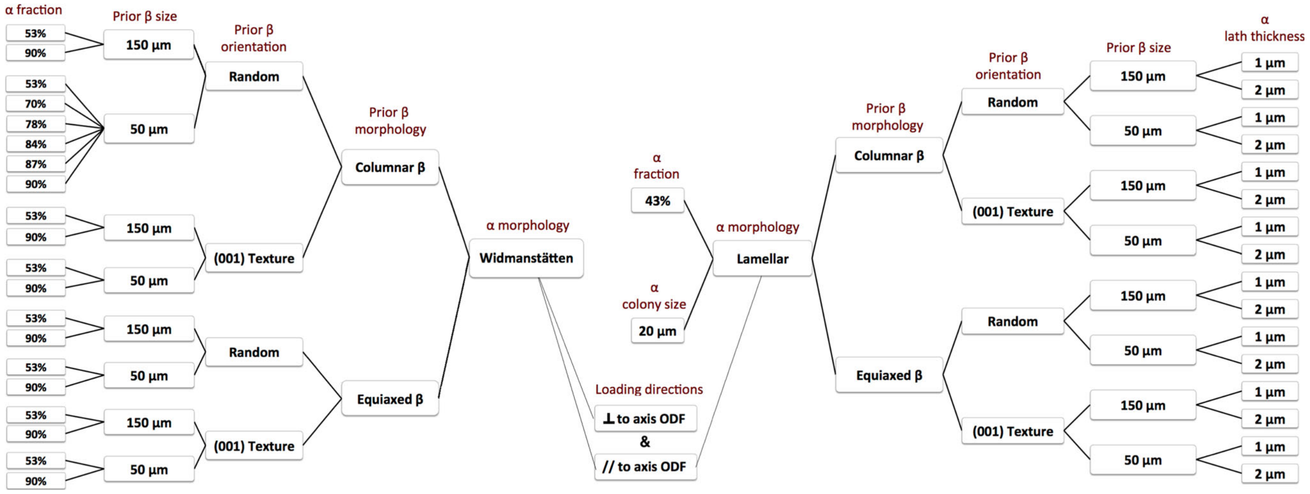

Fig. 8 Simulated 56 conditions for 36 distinct microstructures with varying prior β grain sizes and morphologies, individual α lath thicknesses and sizes, phase volume fractions, and orientation distributions

simply caused by a larger number of harder phase grains. Phase fraction normalized stress–strain distributions showed the lack of a master curve for aggregate behavior. Comparing the stress contributions of different phases for 53, 78 and 90% alpha fraction microstructures, Fig. 10ii, showed that the bcc phase is harder in existence of higher alpha fractions, and it carries the strain while the hcp phase carries the stress. This is in agreement with Dawson et al., who demonstrated that the beta phase is the shear strain carrier, which further increases in magnitude with increased alpha volume fraction [51]. Phase separation analysis also showed the near linear individual contribution of the bcc and hcp phases, which deviates from the linear rule of mixtures for two-phase aggregate response, Fig. 10i. For lower fractions of the harder phase, the aggregate response is controlled by both phases, however as the harder phase fraction increases it dominates the behavior and the importance of the softer phase diminishes. In summary, as the fraction of the harder phase is found to affect the behavior of the entire aggregate non-linearly through neighbor interactions, phase fraction is considered a microstructure descriptor for this study. Consistent with the literature, [48], the results in the linear elastic regime indi-

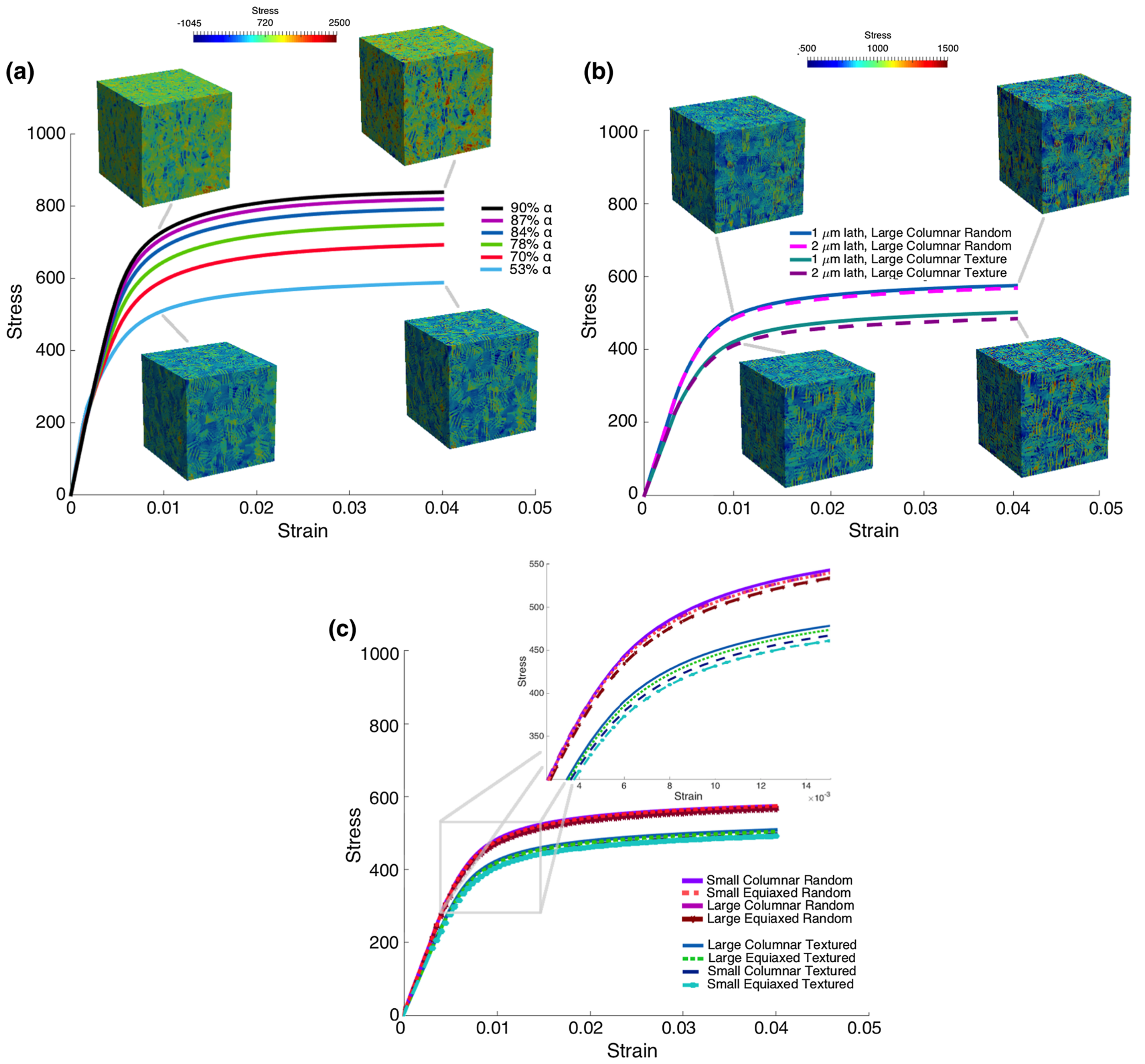

Fig. 9 Microstructure sensitivity analysis. **a** Effect of α fraction; comparison shown for 50 µm randomly oriented columnar prior β parent structures; **b** effect of lath thickness; comparison shown for 150 µm randomly oriented and textured columnar prior β parent structures; **c** effect of prior β grain size, grain morphology and orientation distribution; comparison shown for 53% α Widmanstätten structures

cate an insensitive response to microstructure. However, in the viscoplastic regime, the mechanical behavior is found to be sensitive under all investigated conditions, Figs. 9 and 11.

Figure 11 shows the comparison of the local behavior through violin plots of stress components along the loading direction at 4% strain, for each generated microstructure. The effect of α fraction is depicted in Fig. 11a; for on the x axis 1 denotes loading direction parallel to long grain axis, and 2 denotes loading direction perpendicular to long grain axis. The effect of prior β grain size, grain morphology and orientation distribution is depicted in Fig. 11b; for on the x axis 1 denotes 53% α fraction and loading direction parallel to long grain axis, 2 denotes 53% α fraction and loading direction perpendicular to long grain axis, 3 denotes 90% α fraction and loading direction parallel to long grain axis, and 4 denotes 90% α fraction and loading direction perpendicular to long grain axis. The effect of lath thickness is depicted in Fig. 11c; for on the x axis 1 denotes α lath thickness of 1 µm, and 2 denotes α lath thickness of 2 µm.

The results for both these local, Fig. 11 and the macroscopic, Fig. 9 responses can be summarized as:

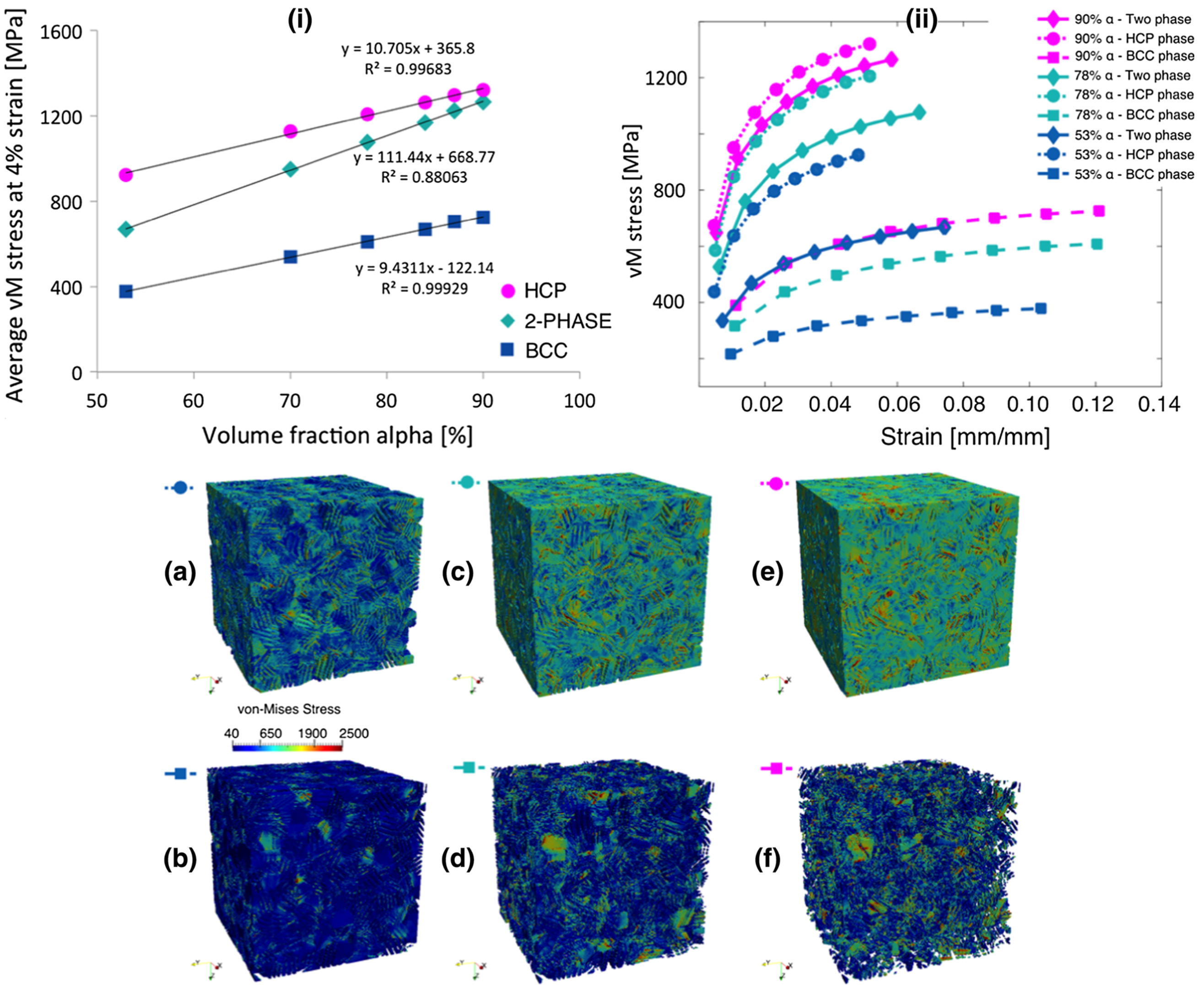

Fig. 10 Average von-Mises stresses carried by the aggregate, bcc and hcp phases as a function of the alpha phase fraction on the *left*, and stress–strain curves for the aggregate, bcc and hcp phases with different α fractions on the *right*. Microstructures **a**, **b** von-Mises stress distributions of the hcp and bcc phases for the 53% α case, **c**, **d** von-Mises stress distributions of the hcp and bcc phases for the 78% α case, **e**, **f** von-Mises stress distributions of the hcp and bcc phases for the 90% α case

i. Effect of α fraction: being the harder phase of two, increase in α fraction increases the tensile strength, Fig. 9a.
ii. Effect of prior β size: for randomly orientated prior β grains, decrease in prior β size increases the tensile strength very slightly. However, as the epitaxial texture strength of the prior β increases, a direct grain size dependence is observed where increase in prior β size increases the tensile strength, both for columnar and equiaxed β morphologies, Fig. 9c.
iii. Effect of prior β morphology: columnar prior β morphology results in a higher yield point and tensile strength as compared to equiaxed grains. The magnitude of difference is found to increase in existence of texture, i.e. difference between columnar grains with (001) texture and equiaxed grains with (001) texture are higher as compared to the difference between their randomly oriented counterparts, Fig. 9c.
iv. Effect of lath thickness: increase in α lath thickness decreases the tensile strength Fig. 9b. Existence of (001) texture intensifies the effect of lath thickness.
v. Effect of loading direction: deformation parallel to long grain axis (axis ODF), which is also the direction of texture fiber, gives marginally higher stress values than texture perpendicular deformation, Fig. 11a. However, the effect of loading direction has the least influence on the behavior when compared with the effect of other descriptors.
vi. Effect of prior β orientation: increase in (001) fiber texture strength decreases the tensile strength, both for when

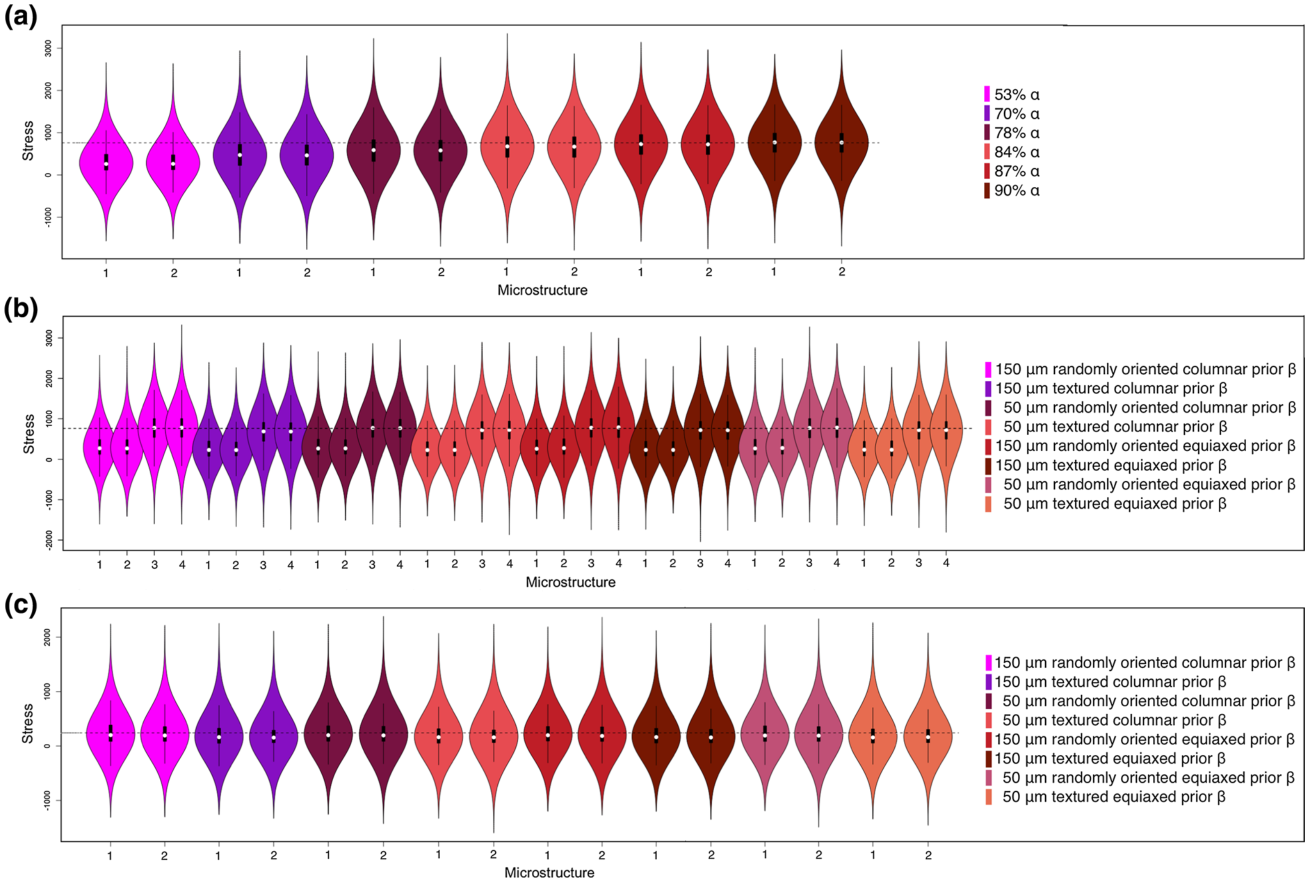

Fig. 11 Violin plots of stress components along the loading direction at 4% strain, for each generated microstructure. **a** Effect of α fraction for 50 µm randomly oriented columnar prior β parent structures. On the x axis, *1* denotes loading direction parallel to long grain axis, *2* denotes loading direction perpendicular to long grain axis; **b** effect of prior β grain size, grain morphology and orientation distribution. On the x axis, *1* denotes 53% α fraction and loading direction parallel to long grain axis, *2* denotes 53% α fraction and loading direction perpendicular to long grain axis, *3* denotes 90% α fraction and loading direction parallel to long grain axis, *4* denotes 90% α fraction and loading direction perpendicular to long grain axis; **c** effect of lath thickness. On the x axis, *1* denotes α lath thickness of 1 µm, *2* denotes α lath thickness of 2 µm

deformation is parallel and perpendicular to the texture fiber direction, Fig. 9c. Although (001) fiber causes a weaker mechanical response, it enhances the effect of other microstructures features for all of the examined conditions, e.g., difference in stress values of columnar vs. equiaxed prior β structures that are randomly oriented or textured, difference in 1 versus 2 µm α lath thickness transformed from randomly oriented or textured prior β etc.

6 Discussion

The spectral full-field FFT based modeling technique was used to quantify partitioning of stress and strain between the harder hcp α phase and softer bcc β phase. Relationships were determined between the alpha fraction/morphology/size, β morphology/size/orientation, loading direction, and the resulting mechanical response in the generated two-phase structures. Some of the results such as the effect of prior beta texture, the alpha fraction and the lamellar alpha configuration agreed with previous work [2,3,7–9,51]. On the other hand, the result on the effect of prior β grain size was not in full agreement with Lutjering's ductility-prior β grain size relationship theory; that proposes the length of the β size as grain boundary α slip length limiting factor, causing reduced stress concentrations for small β grain sizes, higher ductility and lower tensile strength [2,3]. With the utilized rate-sensitive crystal plasticity constitutive equation and the hardening model, a reversed effect is observed for random vs. textured β grains; for the random texture case, the tensile strength increased very slightly (almost negligible) with decreased grain size, whereas for the textured case the tensile strength decreased with decreased grain size. The disagreement with the literature for the randomly oriented prior β case is attributed to the simplicity of the utilized hardening model, where the slip system resistance is not explicitly modified to implement a grain size effect.

7 Conclusion

The studies carried out have established that a computational approach of concurrent synthetic microstructure generation and micromechanical modeling is useful for investigation of microstructure–deformation relationships in polyphase polycrystalline materials. The sensitivity of mechanical properties to several types of microstructural feature can be quantified. Furthermore, the virtual microstructure database that was generated, combined with the corresponding micromechanical data, can be utilized by others for designing new process maps and material systems for additive manufacturing when a particular set of properties are targeted. The results of the present paper is summarized as:

1. The response was the most sensitive to the alpha fraction and prior β texture;
2. Increase in α phase enhanced the tensile strength, as the low temperature α phase is harder than the high temperature β phase;
3. Increased magnitude of prior β (001) texture decreased the tensile strength. This can be explained by the prior β (001) texture being the soft direction for the bcc phase;
4. When α phase was present in lamellar configuration, it dominated the behavior. This amplified the effect of α lath thickness as being inversely related to the tensile strength due to decreased slip length;
5. Columnar prior β grains resulted in higher tensile strength as compared to equiaxed grains.

Acknowledgements This research is supported by the National Science Foundation, under the Award No. DMREF-1435544. For computing resources, this research extensively used local computer clusters and resources of the National Energy Research Scientific Computing Center, a DOE Office of Science User Facility supported by the Office of Science of the U.S. Department of Energy under Contract No. DE-AC02-05CH11231. Dr. Ricardo Lebensohn is acknowledged for his FFT based models and his valuable support on the code/algorithm development.

References

1. Frazier WE (2014) Metal additive manufacturing: a review. J Mater Eng Perform 23(6):1917–28
2. Lutjering G, Williams JC (2003) Titanium. Springer, New York
3. Lutjering G (1998) Influence of processing on microstructure and mechanical properties of $\alpha + \beta$ titanium alloys. Mater Sci Eng A 243(1–2):32–45
4. Semiatin SL, Seetharaman V, Weiss I (1996) The thermomechanical processing of alpha/beta titanium alloys. J Mater 49(6):33–39
5. Kobryn PA, Semiatin SL (2003) Microstructure and texture evolution during solidification processing of Ti–6Al–4V. J Mater Process Technol 135:330–339
6. RMI Titanium Company (2000) Titanium alloy guide. RMI Titanium Company an RTI International Metals, Inc. Company, pp 1–45
7. Zhai Y, Galarraga H, Lados DA (2015) Microstructure evolution, tensile properties, and fatigue damage mechanisms in Ti–6Al–4V alloys fabricated by two additive manufacturing techniques. Procedia Eng 114:658–666
8. Murr LE, Esquivel EV et al (2009) Microstructures and mechanical properties of electron beam-rapid manufactured Ti–6Al–4V biomedical prototypes compared to wrought Ti–6Al–4V. Mater Charact 60:96–105
9. Swarnakar AK, Van der Biest O, Baufeld B (2010) Thermal expansion and lattice parameters of shaped metal deposited Ti–6Al–4V. J Alloys Compd 509(6):2723–28
10. Gockel J, Beuth J (2013) Understanding Ti–6Al–4V microstructure control in additive manufacturing via process maps. In: Solid freeform fabrication proceedings, pp 666–674
11. Bontha S, Klingbeil NW, Kobryn PA, Fraser HL (2009) Effects of process variables and size-scale on solidification microstructure in beam-based fabrication of bulky 3D structures. Mater Sci Eng A 513–514:311–318
12. Beese AM et al (2015) Anisotropic tensile behavior of Ti–6Al–4V components fabricated with directed energy deposition additive manufacturing. Acta Mater 87:309–320
13. Kanit T, Forest S, Galliet I, Mounoury D, Jeulin D (2003) Determination of the size of the representative volume element for random composites: statistical and numerical approach. Int J Solids Struct 40(13–14):3647–3679
14. Fan ZG, Wu Y, Zhao X, Lu Y (2004) Simulation of polycrystalline structure with Voronoi diagram in Laguerre geometry based on random closed packing of spheres. Comput Mater Sci 29(3):301–308
15. Groeber MA, Ghosh S, Uchic MD, Dimiduk DM (2007) Developing a robust 3-D characterization–representation framework for modeling polycrystalline materials. J Mater 59(9):32–36
16. Groeber MA, Ghosh S, Uchic MD, Dimiduk DM (2008) A framework for automated analysis and simulation of 3D polycrystalline microstructures. Part 2: Synthetic structure generation. Acta Mater 56(6):1274–1287
17. Saylor DM, Fridy J, El-Dasher BS, Jung KY, Rollett AD (2004) Statistically representative three-dimensional microstructures based on orthogonal observation sections. Metall Mater Trans A 35A(7):1969–1979
18. Venkataramani G, Kirane K, Ghosh S (2008) Microstructural parameters affecting creep induced load shedding in Ti-6242 by a size dependent crystal plasticity FE model. Int J Plast 24:428–454
19. Thomas J, Groeber M, Ghosh S (2012) Image-based crystal plasticity FE framework for microstructure dependent properties of Ti–6Al–4V alloys. Mater Sci Eng A 553:164–175
20. Zhang M, Zhang J, McDowell DL (2007) Microstructure-based crystal plasticity modeling of cyclic deformation of Ti–6Al–4V. Int J Plast 23:1328–1348
21. Przybyla CP, McDowell DL (2010) Simulation-based extreme value marked correlations in fatigue of advanced engineering alloys. Procedia Eng 2:1045–1056
22. Simonelli M, Tse YY, Tuck C (2012) Further understanding of Ti–6Al–4V selective laser melting using texture analysis. In: Solid freeform fabrication proceedings, pp 480–491
23. Gong X, Lydon J, Cooper K, Chou K (2014) Beam speed effects on Ti–6Al–4V microstructures in electron beam additive manufacturing. J Mater Res 29(17):1951–1959
24. Gong H, Gu H, Zeng K, Dilip JJS et al (2014) Melt pool characterization for selective laser melting of Ti–6Al–4V pre-alloyed powder. In: Solid freeform fabrication proceedings, pp 256–267
25. Nassar AR, Reutzel EW (2015) Additive manufacturing of Ti–6Al–4V using a pulsed laser beam. Metall Mater Trans A 46(6):2781–2789

26. Al-Bermani SS, Blackmore ML, Zhang W, Todd I (2010) The origin of microstructural diversity, texture, and mechanical properties in electron beam melted Ti–6Al–4V. Metall Mater Trans A 41(13):3422–3434
27. Antonysamy AA, Meyer J, Prangnell PB (2013) Effect of build geometry on the β-grain structure and texture in additive manufacture of Ti–6Al–4V by selective electron beam melting. Mater Charact 84:153–168
28. Elmer JW, Palmer TA, Babu SS, Zhang W, DebRoy T (2004) Phase transformation dynamics during welding of Ti–6Al–4V. J Appl Phys 95(12):8327–8339
29. Groeber MA, Jackson M (2014) DREAM.3D: a digital representation environment for the analysis of microstructure in 3D. Integr Mater Manuf Innov 3:5
30. Sachs G (1928) Plasticity problems in metals. Trans Faraday Soc 24:84–92
31. Taylor GI (1938) Plastic strain in metals. J Inst Met 62:307–324
32. Eshelby JD (1957) The determination of the elastic field of an ellipsoidal inclusion and related problems. Proc R Soc Lond Ser A Math Phys Eng Sci A241:376–396
33. Molinari A, Canova GR, Ahzi S (1987) A self consistent approach of the large deformation polycrystal viscoplasticity. Acta Metall 35:2983–94
34. Lebensohn RA, Turner PA, Signorelli JW, Canova GR, Tomé SN (1998) Calculation of intergranular stresses based on a large-strain viscoplastic self-consistent polycrystal model. Model Simul Mater Sci Eng 6(4):447–65
35. Moulinec H, Suquet P (1998) A numerical method for computing the overall response of nonlinear composites with complex microstructure. Comput Methods Appl Mech Eng 157(1–2):69–94
36. Prakash A, Lebensohn RA (2009) Simulation of micromechanical behavior of polycrystals: finite elements versus fast Fourier transforms. Modell Simul Mater Sci Eng 17:064010
37. Lebensohn RA, Liu Y, Castañeda PP (2004) On the accuracy of the self-consistent approximation for polycrystals: comparison with full-field numerical simulations. Acta Mater 52:5347–61
38. Lebensohn RA (2001) N-site modeling of a 3D viscoplastic polycrystal using Fast Fourier Transform. Acta Mater 49: 2723–37
39. Lebensohn RA, Kanjarla AK, Eisenlohr P (2012) An elasto-viscoplastic formulation based on fast fourier transforms for the prediction of micromechanical fields in polycrystalline materials. Int J Plast 32:59–69
40. Mura T (1988) Micromechanics of defects in solids. Martinus-Nijhoff, Dodrecht
41. Lebensohn RA, Tome CN, Ponte CastaNeda P (2007) Self-consistent modelling of the mechanical behaviour of viscoplastic polycrystals incorporating intragranular field fluctuations. Philos Mag 87(28):4287–4322
42. Voce E (1955) A practical strain hardening function. Metallurgia 51:219–226
43. Gockel BT (2016) Constitutive response of a near-alpha titanium alloy as a function of temperature and strain rate. The Ohio State University. Electronic Thesis or Dissertation, Carnegie Mellon University
44. Mandal S, Gockel BT, Balachandran S, Banerjee D, Rollett AD (2017) Simulation of plastic deformation in Ti-5553 alloy using a self-consistent viscoplastic model. Int J Plast 94:57–73
45. Bieler TR, Semiatin SL (2002) The origins of heterogeneous deformation during primary hot working of Ti–6Al–4V. Int J Plast 18(9):1165–1189
46. Facchini L, Magalini M, Robotti P, Molinari A (2009) Microstructure and mechanical properties of Ti–6Al–4V produced by electron beam melting of pre-alloyed powders. Rapid Prototyp J 15(3):171–178
47. Stapleton AM et al (2008) Evolution of lattice strain in Ti–6Al–4V during tensile loading at room temperature. Acta Mater 56:6186–6196
48. Ozturk T et al (2016) Simulation domain size requirements for elastic response of 3D polycrystalline materials. Model Simul Mater Sci Eng 24:015006
49. Werner E, Wesenjak R, Fillafer A, Meier F, Krempaszky C (2016) Microstructure-based modelling of multiphase materials and complex structures. Contin Mech Thermodyn 28:1325–1346
50. Boyle KP, Curtin WA (2005) Grain interactions in crystal plasticity. NUMISHEET2005 778:433–438
51. Barton NR, Dawson PR (2001) On the spatial arrangement of lattice orientations in hot-rolled multiphase titanium. Model Simul Mater Sci Eng 9:433–463